Chemical Science

ROYAL SOCIETY OF CHEMISTRY

EDGE ARTICLE

View Article Online
View Journal | View Issue

Cite this: *Chem. Sci.*, 2022, **13**, 7355

All publication charges for this article have been paid for by the Royal Society of Chemistry

Received 28th March 2022
Accepted 1st June 2022

DOI: 10.1039/d2sc01769e

rsc.li/chemical-science

Zn(II)-Coordination-driven self-assembled nanoagents for multimodal imaging-guided photothermal/gene synergistic therapy†

Hui Hu,‡[a] Nan Yang,‡[b] Jiahui Sun,[a] Fu Zhou,[a] Rui Gu,[b] Yuan Liu,[a] Li Wang,[a] Xuejiao Song,[b] Ruirui Yun,[a] Xiaochen Dong*[b] and Guangfeng Wang*[a]

Synergistic photothermal therapy (PTT) with gene therapy (GT) has drawn emerging interest in the improvement of cancer therapeutic efficiency, while the co-delivery of photothermal agents (PTAs) and therapeutic genes by an integrated nanoplatform, with controllability and biodegradability, is still challenging and urgently desired. Herein, a multi-functional metal–organic framework (MOF) based PTT–GT platform (siRNA@PT-ZIF-8) was developed, which was constructed with siRNA, a near-infrared (NIR) responsive organic dye IR780 derivative (IR780-1), and 2-methylimidazole (2-MIM) by a facile one-pot self-assembly method. This "all-in-one" system of siRNA@PT-ZIF-8 enabled not only photothermal/photoacoustic/fluorescence multimodal imaging but also tumor microenvironment responsiveness for specific and on-demand release of therapeutic cargos, overcoming the inherent limitations of free gene or organic PTA molecules (*e.g.*, short blood circulation half-life and weak stability) in conventional PTT and GT. This nanoplatform provides an efficient and safe strategy for cancer theranostics, and the one-step assembly strategy favors personalized formulation design for diverse demands in cancer management.

Introduction

Near-infrared (NIR) laser-induced photothermal therapy (PTT), employing photothermal agents (PTAs) to generate hyperthermia at tumor sites and cause photothermal ablation of tumor tissues, is a newly updated non-invasive precise cancer therapy, attracting massive attention from researchers.[1–7] Unfortunately, the intense photothermal heating for efficient ablation of tumors unavoidably results in nonspecific damage to surrounding normal tissues and unendurable heat pain in patients.[8–10] Different from traditional PTT, which involves high temperatures (above 50 °C), the emerging mild PTT utilizes lower temperature (~45 °C) for tumor treatment which is safer for normal tissues, thereby exhibiting great potential in clinical applications.[10–18] Nonetheless, mild hyperthermia can also elicit tumor cells' self-protection and turn them immunosuppressive by up-regulating a specific type of protein in tumor cells, such as indoleamine 2,3-dioxygenase, programmed death-ligand 1 (PD-L1), and heat shock proteins (HSPs), leading to therapeutic resistance and severe circumscribing of the therapeutic efficiency.[19–22] Thus, strategies that can improve the therapeutic effect of mild PTT are highly desirable.

Previous studies have demonstrated that coupling gene therapy (GT) with mild PTT is an excellent option to suppress heat resistance and minimize side effects to improve the overall therapeutic outcome.[23–26] However, negatively charged gene molecules suffer from inescapable strong cell membrane repulsion and inherent fragility to nuclease degradation. Therefore, efficient delivery vehicles are necessary to remedy the limitations of free gene molecules and assist them in performing therapeutic tasks inside living cells.[27–32] By virtue of this, the development of effective vehicles enabling co-delivery of PTAs and genes is pivotal for PTT–GT combination therapy.

Up to now, some research revolving around this topic has been reported. For example, multi-functional nanoplatforms based on Au nanorods,[13] zirconium-ferriporphyrin metal–organic frameworks (MOFs),[23] MnO_2,[33] WS_2,[34] black phosphorus,[35] graphene,[36] and carbon nanotubes,[36] have been developed for co-delivery of PTAs and therapeutic gene molecules. Despite encouraging results obtained through these approaches, there are still several stumbling blocks for the clinical translation of PTT–GT strategies: (i) sophisticated synthesis and stepwise modification procedures make the nanoplatforms lack homogeneity and are difficult to produce at

[a]*Key Laboratory of Chem-Biosensing of Anhui Province, Key Laboratory of Functional Molecular Solids, College of Chemistry and Materials Science, Anhui Normal University, Wuhu 241000, Anhui Province, China. E-mail: wangyuz@mail.ahnu.edu.cn*

[b]*Key Laboratory of Flexible Electronics (KLOFE), Institute of Advanced Materials (IAM), Nanjing Tech University (NanjingTech), Nanjing, 211816, China. E-mail: iamxcdong@njtech.edu.cn*

† Electronic supplementary information (ESI) available: Synthesis of IR780-1, experimental details, loading efficiency calculations, additional characterization data, and control results, Fig. S1–S24, Schemes S1, S2, and Movie S1. See https://doi.org/10.1039/d2sc01769e

‡ These authors contributed equally to this work.

a large scale. (ii) Nanovehicles load therapeutic genes on their surface by weak interactions, such as electrostatic attractions or hydrogen bonding, which usually result in insufficient loading capacity and inevitably expose the easily degradable genes to the complex physiological environment. (iii) The weak biodegradability of most inorganic nanovehicles has been a crucial

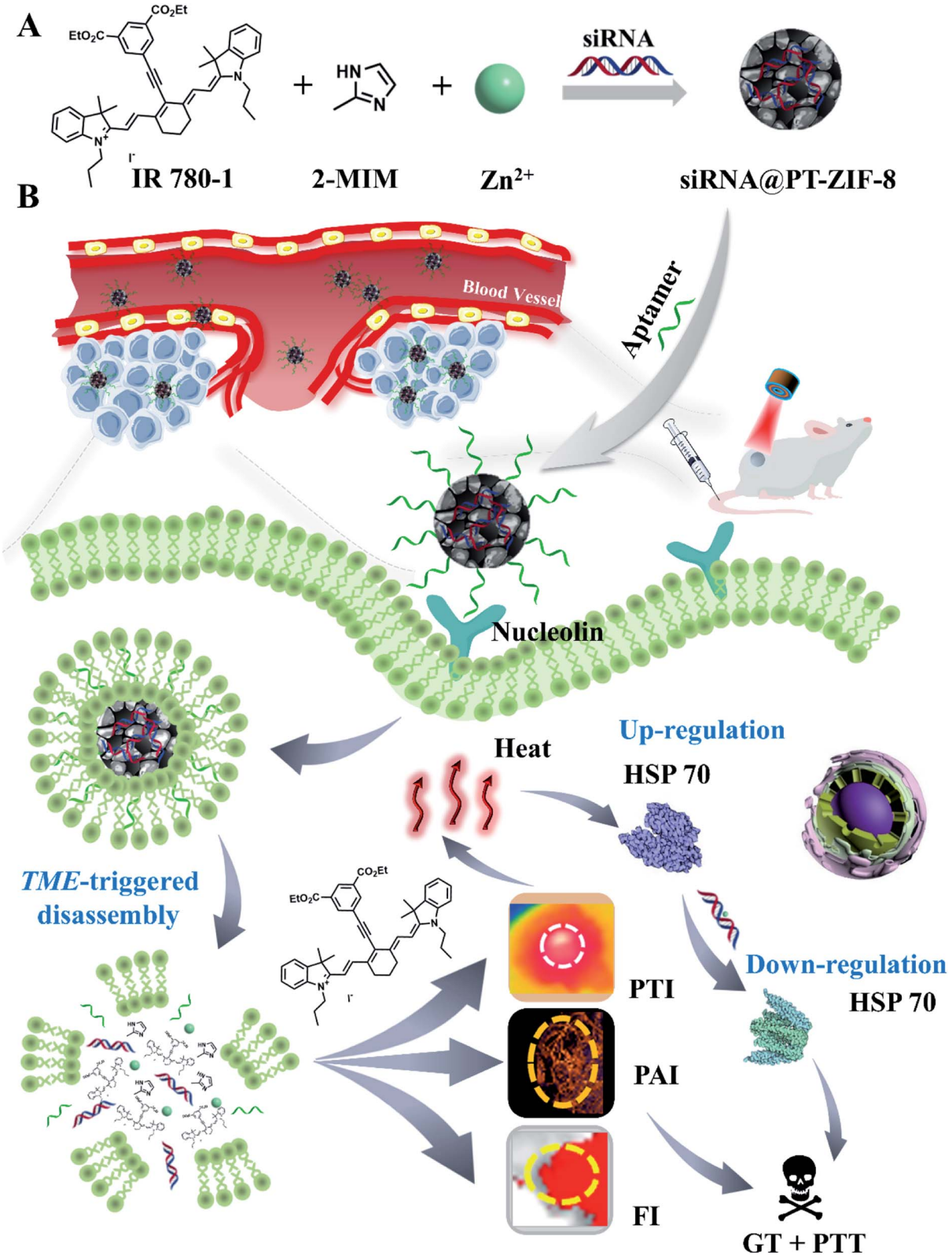

Scheme 1 (A) One-pot self-assembly preparation of siRNA@PT-ZIF-8. (B) Schematic illustration of siRNA@PT-ZIF-8 for tri-modal imaging-guided synergistic mild photothermal and gene therapy.

issue in terms of biosafety. To this end, PTT–GT synergistic strategies should be improved by endowing the co-delivery formulations with simplified synthetic processes, sufficient PTA/gene loading capacity, and good biodegradability.

Recently, metal-coordinated self-assembly involving metal coordination and organic self-assembly has displayed great potential in loading and delivering various functional molecules for biomedical applications.[29,37–39] However, the study on the synergistic PTT–GT by metal-coordinated self-assembly has rarely been reported. Herein, a facile one-pot metal-coordinated self-assembly method is employed to fabricate an "all-in-one" MOF, siRNA@PT-ZIF-8, for multimodal imaging-guided PTT/GT. Within this nanostructure, the NIR responsive organic dye IR780 derivative (denoted as IR780-1) and 2-methylimidazole (2-MIM) act as co-ligands to coordinate with the metal center zinc cations in the presence of siRNA. This nanoassembly is endowed with several advantages: (1) the nanoformulation overcomes the intrinsic limitations of free organic PTAs, such as rapid renal filtration, short blood circulation half-life, photobleaching, and low tissue selectivity. (2) The encapsulation of siRNA into MOFs prevented rapid nuclease degradation and improved its stability during blood circulation. (3) The coordination bond-based tumor microenvironment responsiveness of siRNA@PT-ZIF-8 features selective and on-demand release of therapeutic cargos. (4) The integration of photothermal imaging (PTI), photoacoustic imaging (PAI), and fluorescence imaging (FI) in siRNA@PT-ZIF-8 enables spatiotemporal control on PTT/GT (Scheme 1). This nanoplatform displayed a simple synthesis process, good biodegradability, and a satisfying synergistic mild PTT–GT therapeutic effect.

Results and discussion

First, 5-ethynyl terephthalate was reacted with IR780 to obtain a photothermal ligand IR780-1 for further conjugation with metal ions (Scheme S1†). The formation of IR780-1 can be easily identified by the color of the reaction solution varying from green to purple. Then the products were purified by silica gel

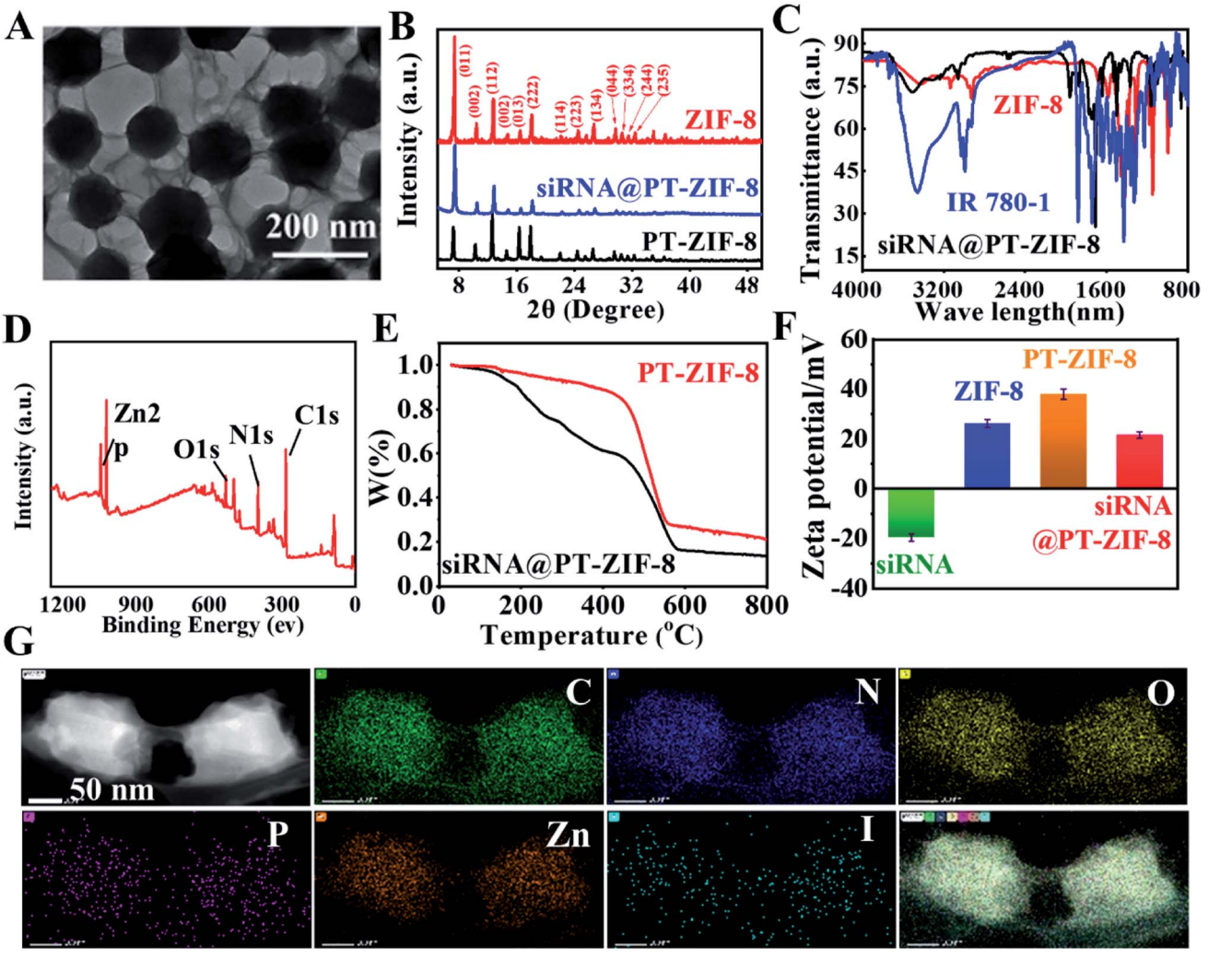

Fig. 1 (A) TEM image of siRNA@PT-ZIF-8. (B) XRD patterns of ZIF-8, PT-ZIF-8, and siRNA@PT-ZIF-8. (C) FTIR spectra of IR780-1, ZIF-8, and siRNA@PT-ZIF-8. (D) XPS spectrum of siRNA@PT-ZIF-8. (E) The thermal gravimetric analysis of PT-ZIF-8 and siRNA@PT-ZIF-8. (F) Zeta potentials of siRNA, ZIF-8, PT-ZIF-8, and siRNA@PT-ZIF-8. (G) Elemental mapping analyses of siRNA@PT-ZIF-8.

column chromatography with a yield of 40.1%. The prepared IR780-1 was characterized by ^{1}H and ^{13}C NMR spectroscopies and electrospray ionization mass spectrometry (ESI-MS) with the $[M + H]^+$ ion at m/z 750.5810 (Fig. S1–S3†), confirming the successful synthesis of the designed PT ligand IR780-1. Additionally, siRNA@PT-ZIF-8 was synthesized by a facile one-pot self-assembly (Scheme 1A), and its controls without the addition of siRNA or IR780-1 (PT-ZIF-8; siRNA@ZIF-8) and the control formed by physical mixing of siRNA and PT-ZIF-8 (siRNA + PT-ZIF-8) were also prepared (Scheme S2†). The structural and componential characteristics of siRNA@PT-ZIF-8 were further investigated. As characterized by transmission electron microscopy (TEM) (Fig. 1A), siRNA@PT-ZIF-8 has polyhedral nanostructures with clear morphology which were epitaxially grown into ultra-thin nanosheets. Furthermore, the TEM elemental mapping images suggest that the N, O, C, P, Zn, and I elements of siRNA@PT-ZIF-8 were uniformly distributed (Fig. 1G). Compared with PT-ZIF-8 (Fig. S4†), the presence of P element in siRNA@PT-ZIF-8 proved that siRNA was successfully integrated. X-ray powder diffraction (XRD) analysis showed that the crystal structures of PT-ZIF-8 and siRNA@PT-ZIF-8 were almost the same as that of the classic ZIF-8 (Fig. 1B), indicating that the loading of siRNA and IR780-1 did not disturb the structure, and the polyhedral nanostructures observed by TEM were mainly from ZIF-8. Additionally, the formation of siRNA@PT-ZIF-8 could also be proved by the Fourier transform infrared (FTIR) spectra. In detail, the presence of the typical vibration bands of IR780-1 (3400 cm^{-1} of =C–H, 3150 cm^{-1} of N–H in the aromatic ring, 2950 and 1450 cm^{-1} of C–H from $-CH_2-$ and $-CH_3$, and 1000 cm^{-1} of $CH-CH_2$) together with those bands corresponding to 2-MIM (1190 cm^{-1} of –C–N) in the FTIR spectra confirmed the presence of IR780-1 and 2-MIM in the siRNA@PT-ZIF-8 framework (Fig. 1C). Meanwhile, the characteristic absorption peak corresponding to the carbonyl group of IR780-1 moved from 1652 cm^{-1} to 1672 cm^{-1} for PT-ZIF-8, implying that the carbonyl group may be involved in the coordination process. The X-ray photoelectron spectroscopy (XPS) survey spectrum in Fig. 1D and S5† exhibits the presence of elements C, N, Zn, and O in the hybrid siRNA@PT-ZIF-8, which coincided with the observation from TEM mapping. In addition, the Zn 2p peaks in siRNA@PT-ZIF-8 were red-shifted compared with those in ZIF-8, implying the possible binding of IR780-1 with Zn^{2+}. Specifically, the electron-absorbing ester group in the IR780-1 organic ligand attenuated the density of the electron cloud around the Zn atom, thereby weakening the shielding effect of external electrons to enhance the binding energy of internal electrons.

Thermal gravimetric analysis (TGA) of PT-ZIF-8 and siRNA@PT-ZIF-8 showed that the mass loss was much more significant when siRNA was embedded than PT-ZIF-8 alone (Fig. 1E), demonstrating that the encapsulated siRNA affected the thermostability of PT-ZIF-8. Compared with ZIF-8, the zeta potential of PT-ZIF-8 increased to +37.5 mV, but siRNA@PT-ZIF-8 displayed a substantially lower zeta potential of +18.6 mV, which is mainly attributed to the incorporated negatively charged siRNA (Fig. 1F). Moreover, the dynamic light scattering (DLS) result showed that the average hydrodynamic size of PT-ZIF-8 slightly increased after the siRNA encapsulation in the framework (Fig. S6†).

To further investigate the spatial distribution of siRNA in the PT-ZIF-8 crystals, siRNA was labeled with green carboxyfluorescein (FAM-siRNA), and its 3D fluorescence images were obtained *via* confocal laser scanning microscopy (CLSM). It was seen that the green fluorescence of FAM-siRNA and red fluorescence of IR780-1 were matched well in siRNA@PT-ZIF-8, which revealed that the FAM-siRNA and IR780-1 dye were well-dispersed throughout the entire PT-ZIF-8 nanoframework (Fig. 2A–C and Movie S1†). In contrast, negligible green fluorescence could be observed if the siRNA molecules were physically mixed with the preformed PT-ZIF-8 (siRNA + PT-ZIF-8) for 30 min (Fig. S7†), suggesting that it was challenging for siRNA to enter the pores of PT-ZIF-8 in a short time.

The loading capacities of IR780-1 and siRNA in siRNA@PT-ZIF-8 were investigated by quantifying IR780-1 or siRNA in the supernatant before and after encapsulation *via* fluorescence spectroscopy. As depicted in Fig. 2D and E, the dispersions of free IR780-1 and FAM-siRNA exhibited apparent fluorescence emission peaking at 620 nm and 525 nm, respectively, while both fluorescence peaks became negligible in the collected supernatant after the self-assembly reaction, implying that the prepared siRNA@PT-ZIF-8 had simultaneously conjugated IR780-1 and siRNA, which was consistent with the conclusion from 3D fluorescence scanning imaging. The loading efficiencies of IR780-1 and siRNA were calculated to be 88.2% and 96.7%, respectively. As a control, the fluorescence of remaining siRNA in the supernatant of siRNA + PT-ZIF-8 and siRNA@ZIF-8 was higher than that of siRNA@PT-ZIF-8 (Fig. 2E), suggesting the effectiveness of biomineralization and the PT ligand in improving the loading capacity of siRNA. The DLS and fluorescence spectra of FAM-siRNA@PT-ZIF-8 dispersed in phosphate buffer (PBS) solutions with pH 7.4 and 5.5 were investigated, respectively. As shown in Fig. S8,† a time-dependent decrease in hydrodynamic size of siRNA@PT-ZIF-8 was observed in the pH 5.5 solution, which could be attributed to the dissociation of coordination bonds between zinc and imidazole in response to the acidic stimulus.[37] In addition, since tumor-targeting specificity of nanomedicines is an essential factor affecting the therapeutic efficacy, a nucleolin-specific aptamer (AS1411), which could target the overexpressed nucleolin on the membrane surface of triple-negative breast cancer cells, was immobilized onto siRNA@PT-ZIF-8 (named Apt/siRNA@PT-ZIF-8). The stability of Apt/siRNA@PT-ZIF-8 was further monitored by UV-vis spectroscopy.[40] When different concentrations of Apt/siRNA@PT-ZIF-8 (0, 40, 80, 120, 160, and 200 μg mL^{-1}) were incubated with PBS (Fig. S9A†) and Dulbecco's Modified Eagle Medium (DMEM) containing 10% FBS (Fig. S9B†), the corresponding hydrodynamic size observed is shown in Fig. S10.† There was no apparent change in the fluorescence spectrum of the Apt/siRNA@PT-ZIF-8 supernatant before and after the NIR laser irradiation for 5 min (Fig. S11a†). Moreover, less than 10% of IR780-1 was leaked in the supernatant from Apt/siRNA@PT-ZIF-8 after a 12 h incubation in PBS (pH = 7.4) (Fig. S11b†), indicating that IR780-1 conjugated stably in Apt/siRNA@PT-ZIF-8.

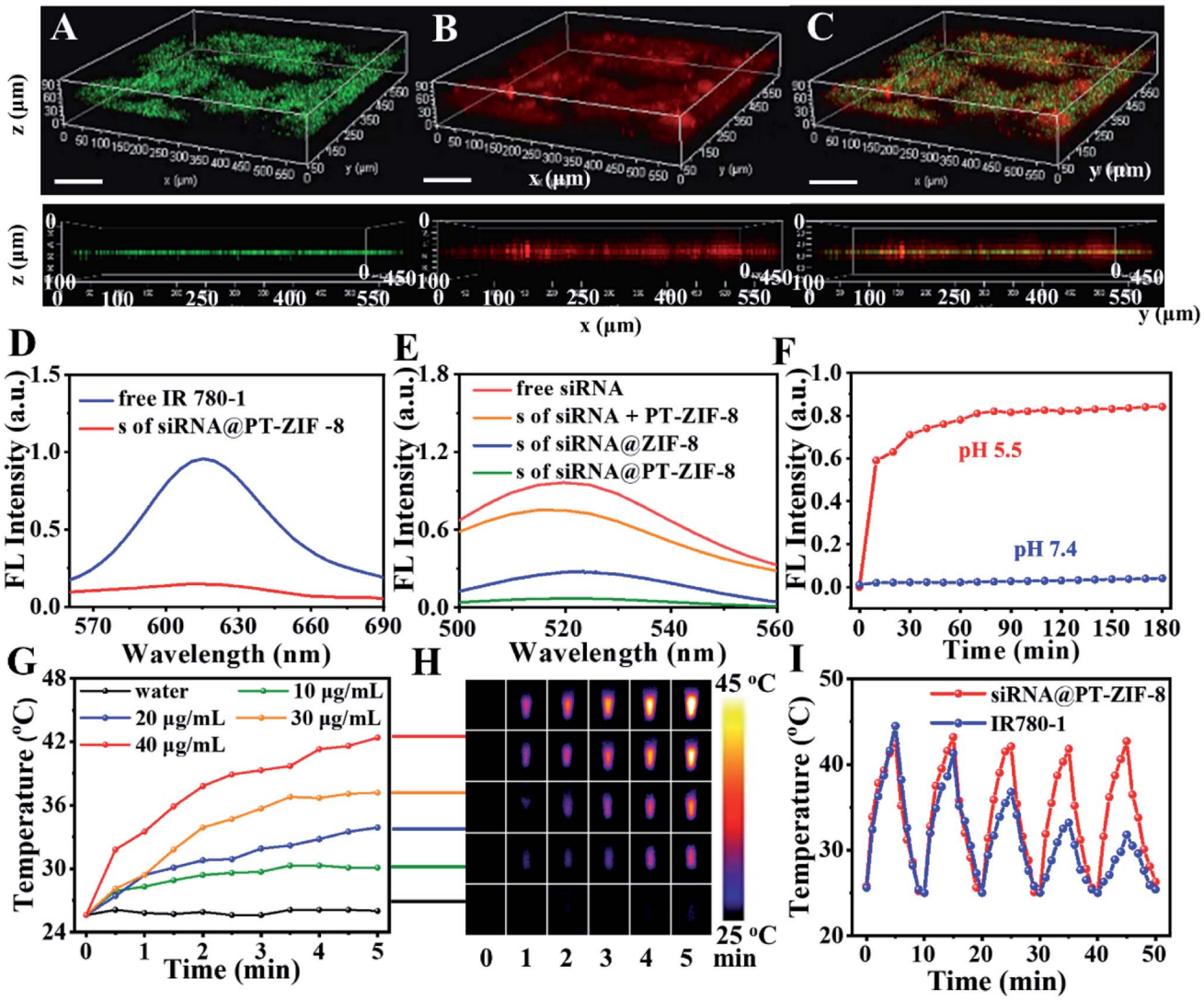

Fig. 2 (A–C) 3D fluorescence images at the *Z*-section and along with *XZ* cross-sectional analysis of siRNA@PT-ZIF-8 based on green fluorescence of FAM-siRNA, red fluorescence of IR780-1, and their merged fluorescence of CLSM. Scale bar: 100 μm. (D) Fluorescence spectra of IR780-1 and the supernatant (abbreviated as "s") of siRNA@PT-ZIF-8. (E) Fluorescence spectrum of FAM-siRNA in different groups. (F) The fluorescence intensity of FAM-siRNA released from FAM-siRNA@PT-ZIF-8 in pH 5.5 or 7.4 PBS solution (n = 3, mean SD). (G) Photothermal curves of different concentrations of siRNA@PT-ZIF-8 under laser irradiation. (H) The corresponding infrared thermography images. (I) Temperature profiles of siRNA@PT-ZIF-8 and IR780-1 irradiated by using an 808 nm laser at 2 W cm^{-2}, followed by natural cooling with laser turn-off.

As shown in Fig. S12,† no obvious change in size and shape of the nanoparticles was observed after incubating in PBS at pH = 7.4 for 7 days, confirming that these assembled nanoparticles were stable at neutral pH, while the nanocomposites decomposed gradually after being incubated with solutions with increased acidity due to the protonation of imidazole group. Furthermore, as validated by the fluorescence spectra in Fig. 2F and S13,† under the neutral conditions, the fluorescence intensity at 525 nm of the FAM-siRNA@PT-ZIF-8 dispersion has no change within 180 min. In contrast, significant fluorescence recovery was observed at pH 5.5 within 10 minutes, originating from the release of FAM-siRNA. Therefore, it was demonstrated that siRNA@PT-ZIF-8 enabled not only the efficient encapsulation of siRNA inside the nanoframework *via* biomimetic mineralization but also the selective and quick release of siRNA under acidic conditions. Furthermore, the protective effect of PT-ZIF-8 on siRNA against RNase A degradation was investigated by agarose gel electrophoresis (Fig. S14†). The band of naked siRNA became weak after the RNase A treatment (lane 1, 4.201 μg mL^{-1}; 2, 3.271 μg mL^{-1}). In contrast, the group of siRNA@PT-ZIF-8 after RNase A treatment remained bright, indicating the protective effect of PT-ZIF-8 on siRNA (lane 3, 9.981 μg mL^{-1}). Additionally, the band of siRNA@PT-ZIF-8 showed apparent retention around the sample, suggesting that siRNA was well-bonded PT-ZIF-8. A less bright band was observed in the siRNA@ZIF-8 group (lane 4, 5.752 μg mL^{-1}). This could be explained by the slightly decreased binding affinity between siRNA and the nano-vehicle due to the absence

of IR780-1. Furthermore, compared to siRNA@PT-ZIF-8 treated with RNase I under neutral conditions (lane 5, 8.806 μg mL^{-1}), a faint band appeared under the acidic conditions (lane 6, 3.223 μg mL^{-1}), suggesting the acidity-responsive release of siRNA from siRNA@PT-ZIF-8. These results implied that PT-ZIF-8 could effectively prevent undesired pre-leakage of siRNA, protect siRNA from degradation, and selectively liberate siRNA in response to acidity, providing an effective strategy for gene delivery and acidic tumor microenvironment-responsive gene therapy.

Furthermore, the photothermal performance of siRNA@PT-ZIF-8 was evaluated using a laser with a power density of 2 W cm^{-2}. As shown in Fig. 2G, siRNA@PT-ZIF-8 exhibited typical concentration-dependent photothermal transduction efficiency. Moreover, the temperature of the siRNA@PT-ZIF-8 dispersion (40 μg mL^{-1}) increased by 17 °C upon 300 s irradiation. The photothermal conversion efficiency of siRNA@PT-ZIF-8 was calculated to be 26.61% (Fig. S15†).[41] For a more intuitive observation, infrared thermal images of the samples during laser irradiation were also recorded (Fig. 2H). In addition, siRNA@PT-ZIF-8 displayed high photothermal stability, with almost the same temperature increments during five consecutive on/off cycles of laser irradiation (Fig. 2I). However, the photothermal stability of the free IR780-1 solution was poor, and the heating efficiency was significantly decreased after two cycles of treatment. The stability of Apt/siRNA@PT-ZIF-8 under laser irradiation was also investigated. There was no apparent change in the fluorescence spectrum of the Apt/siRNA@PT-ZIF-8 supernatant before and after the NIR laser irradiation for 5 min (Fig. S16A†). Moreover, less than 10% of IR780-1 was leaked in the supernatant from Apt/siRNA@PT-ZIF-8 after a 12 h incubation in PBS (pH = 7.4), indicating that IR780-1 conjugated stably in Apt/siRNA@PT-ZIF-8 (Fig. S16B†). Therefore, Apt/siRNA@PT-ZIF-8 had potential application in PTT because of its excellent photothermal conversion performance and stability.

A cellular colocalization study was further conducted by co-incubating 4T1 cells (mouse breast cancer cells) with Apt/siRNA@PT-ZIF-8. The CLSM images revealed that the nanocomposites were mainly distributed in the cytoplasm, and the red fluorescence from IR780-1 overlapped well with green fluorescence from the FAM-siRNA probe (overlap coefficient = 0.80) (Fig. S17†). In addition, free IR780-1 and siRNA@PT-ZIF-8 were incubated with 4T1 cells for 12 hours to evaluate the cancer cell targeting ability of the aptamer, and the IR780-1 fluorescence was recorded. As shown in Fig. 3A and B, compared with the free IR780-1 treated cells, the siRNA@PT-ZIF-8 treated group displayed enhanced fluorescence.

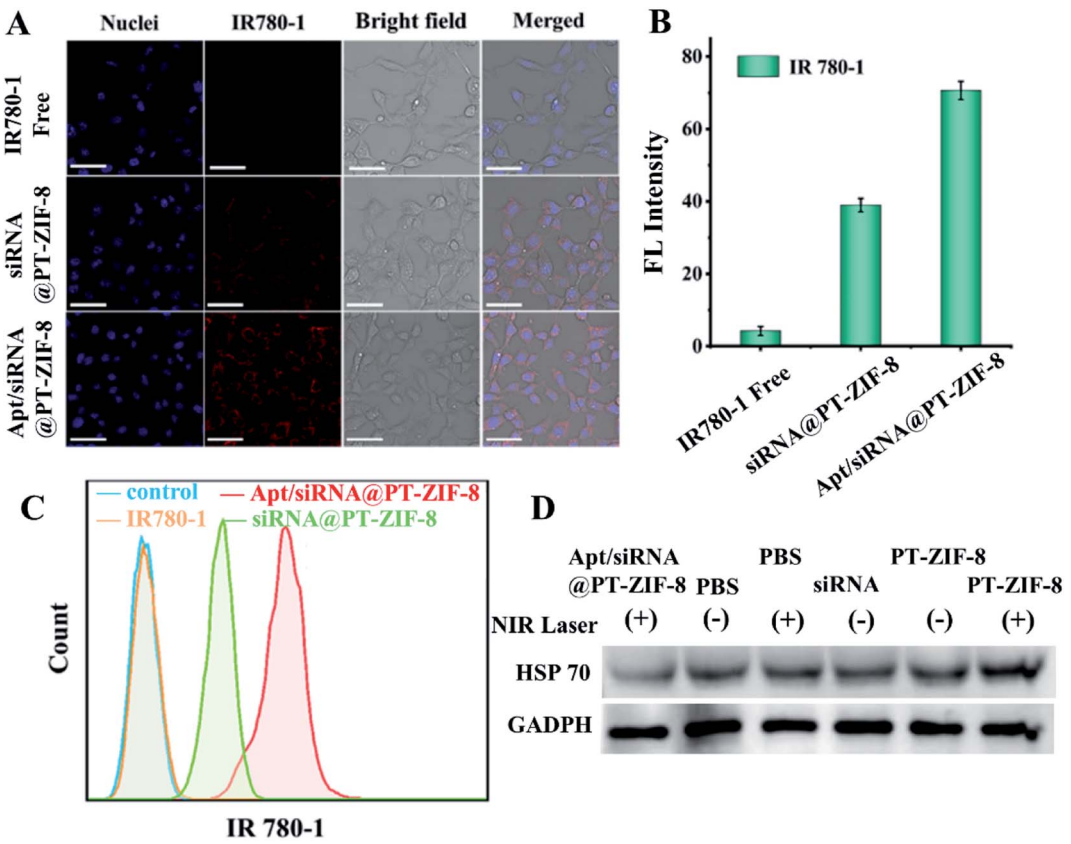

Fig. 3 Cellular uptake analysis of different agents in 4T1 cells. (A) CLSM images and (C) flow cytometry analysis of cellular uptake of IR780-1, siRNA@PT-ZIF-8, and Apt/siRNA@PT-ZIF-8 at a concentration of 50 μg mL^{-1} for 12 h, respectively. Scale bar: 50 μm. (B) The average fluorescence intensity of IR780-1 in 4T1 cells after incubation of 4T1 with different agents for 12 h. (D) Western blot assay of the HSP70 protein from differently treated 4T1 cells: (1) Apt/siRNA@PT-ZIF-8 + NIR, (2) PBS, (3) PBS + NIR, (4) siRNA, (5) PT-ZIF-8, and (6) PT-ZIF-8 + NIR.

Comparatively, the intensity of the red signal was further increased for Apt/siRNA@PT-ZIF-8, indicating that Apt/siRNA@PT-ZIF-8 had higher cellular uptake efficiency than siRNA@PT-ZIF-8. Furthermore, the aptamer promoted cellular uptake of Apt/siRNA@PT-ZIF-8 was confirmed by flow cytometry analysis (Fig. 3C).

Since the expression of a heat shock protein (*e.g.* HSP70) would be improved rapidly upon exposure to hyperthermia in the process of PTT, to inhibit tumor thermoresistance, anti-HSP70 siRNA was used to down-regulate HSP70. The expression of HSP70 in 4T1 cells was explored by western blot analysis (Fig. 3D and S18†). Compared to the control group (PBS), there was no inhibitory effect on HSP70 expression by PBS + NIR. At the same time, the HSP70 level was significantly increased in the PT-ZIF-8 + laser group due to the photothermal effect induced. Notably, compared to the free siRNA treated group, Apt/siRNA@PT-ZIF-8 + NIR treatment downregulated the expression of HSP70 remarkably, which could be explained by the protective effect of PT-ZIF-8 on siRNA and the efficient delivery of siRNA into cancer cells by Apt immobilized PT-ZIF-8.[9] The HSP70 protein expression level decreased significantly after treatment with GT + PTT, because the siRNA down-regulated the HSP70 expression and reduced the heat resistance of cancer cells, consequently making the cells sensitive to heat at relatively mild temperature. These results confirmed the silencing impact of Apt/siRNA@PT-ZIF-8 on the HSP70 gene, which could be integrated with PTT for synergistic cancer therapy.

Inspired by the excellent photothermal conversion efficiency and gene silencing performances of the Apt/siRNA@PT-ZIF-8 nanoplatform, the combined therapeutic efficiency was then explored in 4T1 cells. First, the cytotoxicity was evaluated through CCK-8 analysis. No apparent dark cell toxicity was observed in PT-ZIF-8, siRNA@PT-ZIF-8, or the Apt/siRNA@PT-ZIF-8 group even at a relatively high dosage (with equivalent concentrations of siRNA, IR780-1, and ZIF-8), suggesting excellent biocompatibility of these nanoplatforms (Fig. 4A–C). Nearly no obvious cytotoxicities of Apt/siRNA@PT-ZIF-8 related to different cell lines: 4T1, human cervical carcinoma HeLa, mouse pulmonary fibroma L929 and human alveolar epithelial cell line A549 were observed even when their concentrations were 50 μg mL^{-1} (Fig. S19†), while upon 808 nm laser irradiation, the cell viability in PT-ZIF-8, siRNA@PT-ZIF-8, and Apt/siRNA@PT-ZIF-8 treated groups were all decreased. More impressively, the 808 nm laser irradiated Apt/siRNA@PT-ZIF-8 system displayed the best therapeutic effect among all of these different treatments, which illustrated the many combinational therapeutic performances of PTT and GT *in vitro*. In addition, Apt/siRNA@PT-ZIF-8 showed higher cytotoxicity and an excellent gene silencing effect on 4T1 cells compared with siRNA@PT-ZIF-8 (Fig. 4D). This could be attributed to the higher cellular internalization of Apt/siRNA@PT-ZIF-8 by Apt-mediated targeting recognition of the aptamer on the surface of the 4T1 tumor cells. The photothermal and gene therapy effects of Apt/siRNA@PT-ZIF-8 on 4T1 cells were confirmed intuitively by staining living/dead cells with calcein AM and

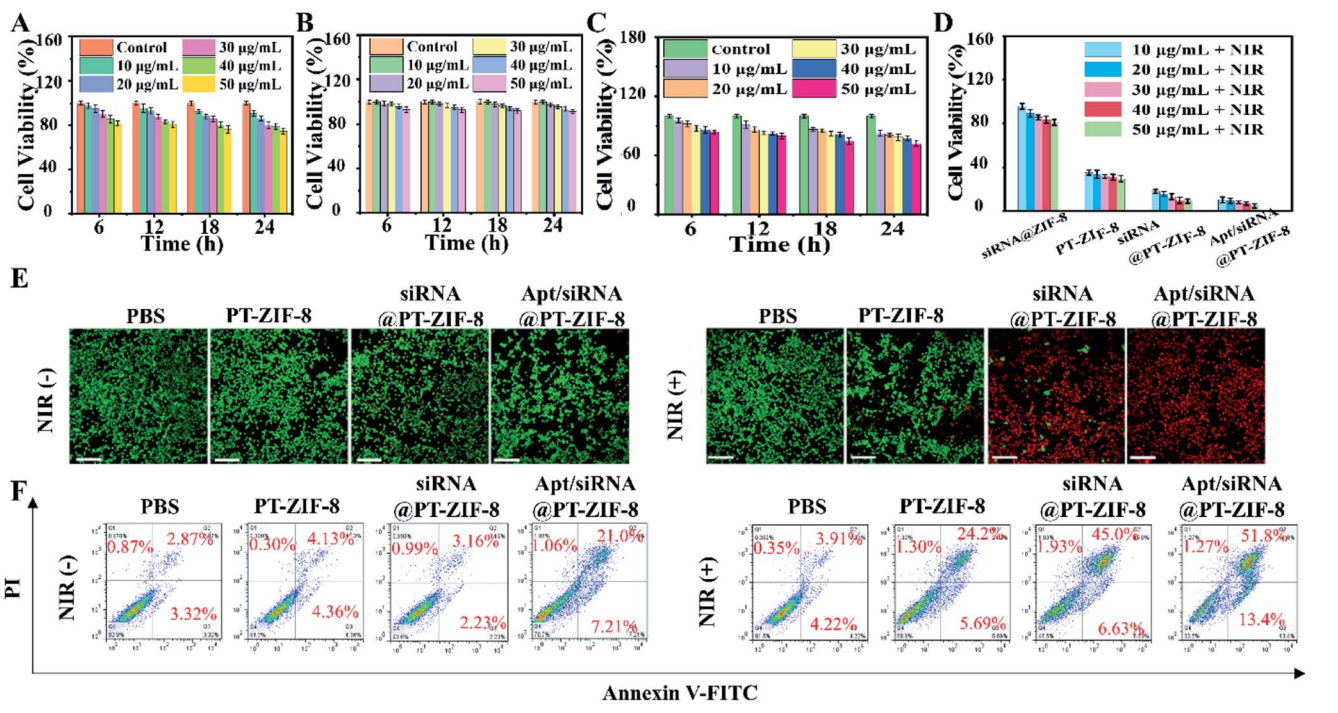

Fig. 4 *In vitro* therapeutic performance of Apt/siRNA@PT-ZIF-8 for 4T1 cells. Viability of 4T1 cells after treatment with (A) PT-ZIF-8, (B) siRNA@PT-ZIF-8, (C) Apt/siRNA@PT-ZIF-8 without or (D) with laser irradiation for 5 min (808 nm, 2 W cm^{-2}). (E) Live/dead cell staining analysis of the differently treated cells. CLSM images of calcein AM (green, live cells) and propidium iodide (red, dead cells) co-stained 4T1 cells treated with PBS, PT-ZIF-8, siRNA@PT-ZIF-8, and Apt/siRNA@PT-ZIF-8 at a concentration of 50 μg mL^{-1}, without or with laser irradiation (808 nm, 2 W cm^{-2}). Scale bar: 100 μm. (F) Flow cytometry assays of 4T1 cells pre-incubated with Annexin V-FITC and PI dyes.

propidium (PI). The confocal laser scanning microscopy (CLSM) images in Fig. 4E clearly show that at a safe power density threshold of an 808 nm laser (2 W cm^{-2}), effective cell ablation could be achieved in cells treated with 50 μg mL^{-1} siRNA@PT-ZIF-8 and Apt/siRNA@PT-ZIF-8. In addition, a distinct trend of early apoptosis of 4T1 cells was identified in flow cytometry analysis after incubation with different formulas plus laser irradiation (Fig. 4F). No significant cytotoxicity was observed in other control groups (PBS, PBS + NIR, PT-ZIF-8, and siRNA@PT-ZIF-8), consistent with the CCK-8 results, signifying that the PTT/GT combined treatment considerably reduced cell activity compared with GT or PTT alone. Meanwhile, the Apt/siRNA@PT-ZIF-8 system with 808 nm laser irradiation displayed the highest anti-tumor efficacy because of the highly efficient delivery and release of IR780-1 and siRNA in 4T1 cells, which led to HSP70 down-regulation for reinforced PTT efficacy. These were explicitly demonstrated *in vitro*.

Taking advantage of the photoacoustic and optical properties of IR780-1, PAI and FI were used to track the *in vivo* biodistribution of Apt/siRNA@PT-ZIF-8 at different time points (Fig. 5A and C). The corresponding 24 h PA and fluorescence intensities at tumor sites were quantified. As shown in Fig. 5B and D, Apt/siRNA@PT-ZIF-8 reached the maximum accumulation in the tumor region at 8 h after intravenous (i.v.) injection. The biodistribution of Apt/siRNA@PT-ZIF-8 was obtained for *ex vivo* fluorescence imaging (Fig. S20†), indicating the high tumor uptake of Apt/siRNA@PT-ZIF-8. At 24 h after i.v. injection, the mice were executed, and the major organs were collected for fluorescence imaging, which indicated a relatively high tumor uptake of Apt/siRNA@PT-ZIF-8. At 8 h post-injection, the *in vivo* photothermal effect of Apt/siRNA@PT-ZIF-8 was evaluated by monitoring temperature variation in tumor regions under 808 nm irradiation (10 min, 2 W cm^{-2}). As seen in Fig. 5E and F, the temperature at the tumor site increased to 38 °C in the control group. In comparison, the Apt/siRNA@PT-ZIF-8 group displayed a rapid temperature increase to almost 48 °C under the same irradiation conditions, indicating that siRNA@PT-ZIF-8 possessed an excellent photothermal conversion capability which could rapidly induce mild PTT *in vivo* for tumor treatment. Then, the anti-tumor efficacy of Apt/siRNA@PT-ZIF-8 was investigated. The mice bearing 4T1 tumors were divided into six groups randomly: PBS, PBS + NIR, siRNA@PT-ZIF-8, siRNA@PT-

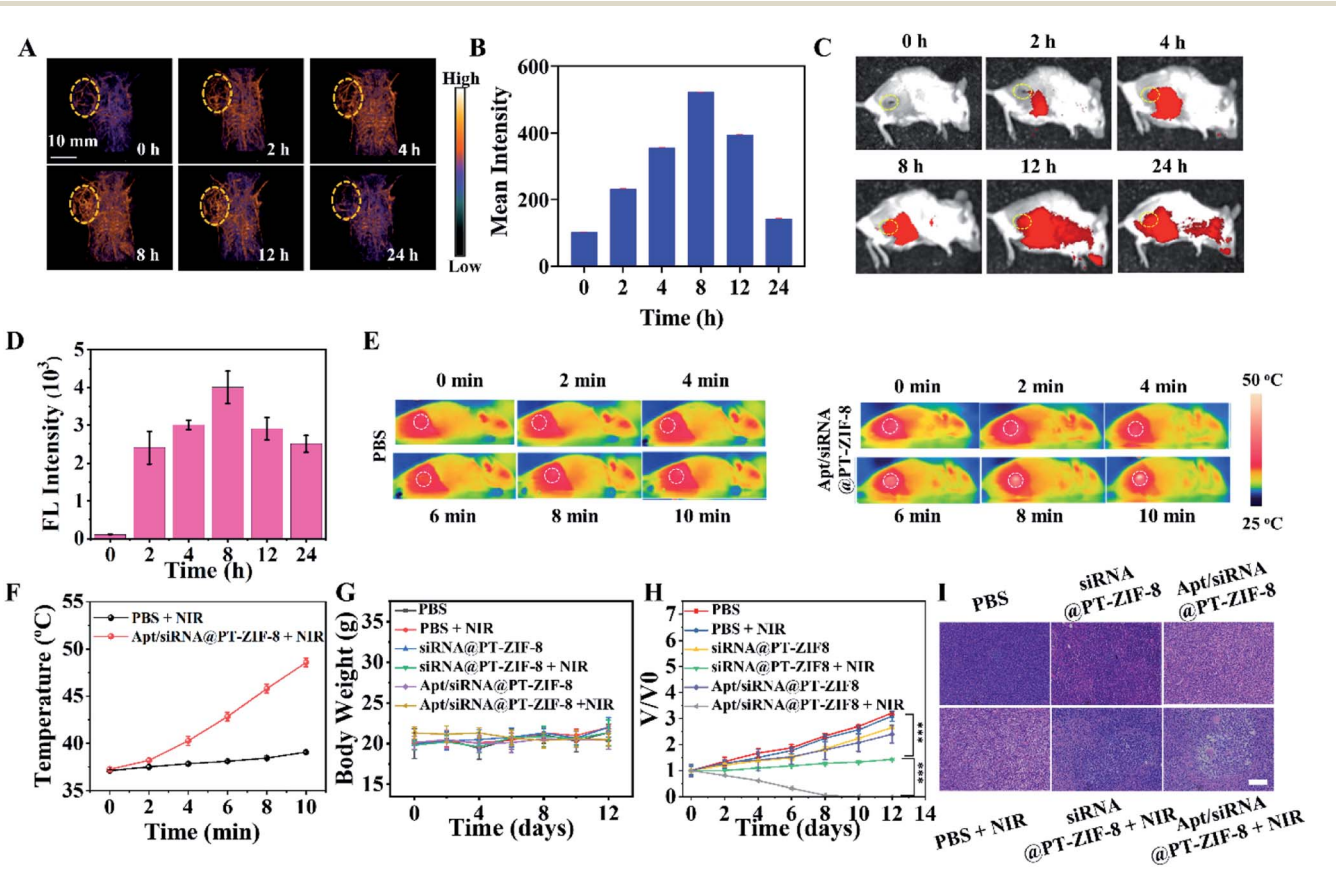

Fig. 5 (A, C) *In vivo* photoacoustic and fluorescence imaging of tumor-bearing mice after i.v. injection of Apt/siRNA@PT-ZIF-8 for 0, 2, 4, 8, 12, and 24 h. (B) The corresponding photoacoustic signal intensity in (A). (D) FI intensity of (C). (E) Thermal IR images of mice treated with PBS or Apt/siRNA@PT-ZIF-8 under 808 nm irradiation (2 W cm^{-2} for 2, 4, 6, 8, and 10 min). (F) Temperature changes on tumor sites according to the imaging in (E), PBS + NIR in the black line, and Apt/siRNA@PT-ZIF-8 + NIR in the red line. (G) Bodyweight monitoring during the process of (a) PBS, (b) PBS + NIR, (c) siRNA@PT-ZIF-8, (d) siRNA@PT-ZIF-8 + NIR, (e) Apt/siRNA@PT-ZIF-8, and (f) Apt/siRNA@PT-ZIF-8 + NIR groups. (H) Tumor volume change curves and all statistical data were represented as mean standard deviation ($n = 4$). (I) Representative H&E staining of the tumor slices collected from the mice on day 2. Scale bar: 100 μm.

ZIF-8 + NIR, Apt/siRNA@PT-ZIF-8, and Apt/siRNA@PT-ZIF-8 + NIR, respectively. Body weights and tumor volumes of the mice were monitored every other day. The body weights in groups with various treatments showed no noticeable change, illustrating the negligible adverse influence of the therapeutic strategies on mice (Fig. 5G). The tumor volumes in the comparative groups rapidly increased in 12 days (Fig. 5H). In contrast, the Apt/siRNA@PT-ZIF-8 + NIR group displayed the most efficient anti-tumor effect, of which complete tumor regression was achieved in all the animal models. This may be because AS1411 bonded specifically to nucleolin at the surface of cancer cells and triggered the PTT–GT reagent release into the cell, and meanwhile, the aptamer AS1411 targeted nucleolin may induce *bcl-2* mRNA instability and cytotoxicity resulting in the tumor cell death.[40] After 12 days of treatment, all mice in the six groups were euthanized, and the tumor tissues were resected (Fig. S21†). Additionally, the hematoxylin and eosin (H&E) stained tumor tissue slices further confirmed the effects of different treatments (Fig. 5I). Compared with other formulation-treated groups, the Apt/siRNA@PT-ZIF-8 + NIR group showed the most severe cell nuclear shrinkage, fragmentation, and condensation. Moreover, *in vivo* pharmacokinetic studies were carefully carried out to explore the blood circulation by measuring the content of Zn in the blood samples collected from a posterior ocular vein of mice at different time intervals after i.v. injection of Apt/siRNA@PT-ZIF-8 NPs. The time-dependent concentration change of Zn could be fitted with the model, and the diffusion and elimination half-times were calculated to be about 0.765 h (Fig. S22†). The above results indicated that Apt/siRNA@PT-ZIF-8-based mild PTT/GT synergistic therapy could effectively induce anti-tumor effects *in vivo* and obtained practical low-temperature PTT effects by silencing genes that induced tumor cell apoptosis and drug resistance-related genes. The blood biochemistry assays also evaluated the biosafety. As shown in Fig. S23A–E,† no apparent hepatic and renal toxicities were observed on days 0, 1, 3, 7, and 15 post i.v. injection. Further, we also detected myocardial injury markers (Fig. S23F†) creatine kinase (CK), creatine kinase isoenzyme (CK-MB), and lactate dehydrogenase 1 (LDH1). This revealed no acute damage after treatment with Apt/siRNA@PT-ZIF-8, further indicating its biosafety. Moreover, at 24 h post i.v. administration to healthy tumor-bearing mice, histological analysis of significant organs was also performed. The significant organs from mice injected with PBS (as a control), and varying formulas were investigated to assess the potential toxicity. The H&E staining results (Fig. S24†) showed that the heart, liver, spleen, lung, and kidney tissues were nearly identical to the tissue samples from healthy controls in terms of the overall structure, integrity, and immune infiltrate levels. These results further indicated the biosafety of Apt/siRNA@PT-ZIF-8 based treatment.

Conclusions

In conclusion, we have developed a one-step assembly strategy for the preparation of a siRNA encapsulated IR780-1 incorporated MOF, siRNA@PT-ZIF-8. With the excellent photochemical/photophysical properties of IR780-1 and siRNA-mediated HSP70 down regulation, the nanoplatform enabled a tri-modal imaging-guided, tumor acidity-triggered PTT–GT combination therapy. Furthermore, active targeting to cancer cells was achieved by aptamer modification. Ultimately, the therapeutic outcome was improved considerably both *in vitro* and *in vivo*, which was attained by the effective delivery and pH-programmed release of therapeutic siRNA and the photothermal agent IR780-1. Further, it is proposed that the one-step assembly strategy could be extended to other theranostic applications by varying the assembly units, thus better meeting the needs of personalized medicine.

Statistics

The data were presented as mean ± standard deviation (SD) unless otherwise stated. To test the significance of the observed differences between the study groups, analysis by variance statistics was applied, and a value of $P < 0.05$ was considered statistically significant ($^{*}p < 0.05$, $^{**}p < 0.01$, and $^{***}p < 0.001$).

Data availability

All the data supporting the findings of this study are available within the article and its ESI files †and from the corresponding author upon reasonable request.

Author contributions

X. D. and G. W.: conceptualization, methodology and funding acquisition; H. H., N. Y., R. G., Y. L., L. W., R. Y., and X. S.: investigation, formal analysis, and visualization; Y. L.: resources; N. Y., F. Z., G. W., and X. D.: data curation and writing – review & editing. All authors discussed the results and commented on the manuscript.

Conflicts of interest

The authors declare no competing financial interest.

Acknowledgements

This work was financially supported by the National Natural Science Foundation of China (Grants 21675001 and 21976004), the key project of the National Natural Science Foundation of China (21936001), and the Natural Science Foundation of Anhui Province (KJ2017A315).

References

1 P. C. Ray, S. A. Khan, A. K. Singh, D. Senapati and Z. Fan, *Chem. Soc. Rev.*, 2012, **41**, 3193.
2 J. Nam, S. Son, K. S. Park, W. Zou, L. D. Shea and J. J. Moon, *Nat. Rev. Mater.*, 2019, **4**, 398–414.
3 H. Sun, Q. Zhang, J. Li, S. Peng, X. Wang and R. Cai, *Nano Today*, 2021, **37**, 101073.

4 S. Liu, X. Pan and H. Liu, *Angew. Chem., Int. Ed.*, 2020, **59**, 5890–5900.
5 P. K. Jain, X. Huang, I. H. El-Sayed and M. A. El-Sayed, *Acc. Chem. Res.*, 2008, **41**, 1578–1586.
6 Z. Jiang, C. Zhang, X. Wang, M. Yan, Z. Ling, Y. Chen and Z. Liu, *Angew. Chem., Int. Ed.*, 2021, **60**, 22376–22384.
7 N. Yang, C. Cao, H. Li, Y. Hong, Y. Cai, X. Song, W. Wang, X. Mou and X. Dong, *Small Struct.*, 2021, **2**, 2100110.
8 Y. Liu, P. Bhattarai, Z. Dai and X. Chen, *Chem. Soc. Rev.*, 2019, **48**, 2053–2108.
9 M. Chang, Z. Hou, M. Wang, C. Yang, R. Wang, F. Li, D. Liu, T. Peng, C. Li and J. Lin, *Angew. Chem., Int. Ed.*, 2021, **60**, 12971–12979.
10 X. Zhang, J. Du, Z. Guo, J. Yu, Q. Gao, W. Yin, S. Zhu, Z. Gu and Y. Zhao, *Adv. Sci.*, 2019, **6**, 1801122.
11 G. Gao, X. Sun and G. Liang, *Adv. Funct. Mater.*, 2021, **31**, 2100738.
12 B.-K. Jung, Y. K. Lee, J. Hong, H. Ghandehari and C.-O. Yun, *ACS Nano*, 2016, **10**, 10533–10543.
13 X. Li, Y. Pan, C. Chen, Y. Gao, X. Liu, K. Yang, X. Luan, D. Zhou, F. Zeng, X. Han and Y. Song, *Angew. Chem., Int. Ed.*, 2021, **60**, 21200–21204.
14 J. Zhou, M. Li, Y. Hou, Z. Luo, Q. Chen, H. Cao, R. Huo, C. Xue, L. Sutrisno, L. Hao, Y. Cao, H. Ran, L. Lu, K. Li and K. Cai, *ACS Nano*, 2018, **12**, 2858–2872.
15 N. Yang, T. Zhang, C. Cao, G. Mao, J. Shao, X. Song, W. Wang, X. Mou and X. Dong, *Nano Res.*, 2022, **15**, 2235–2243.
16 N. Yang, H. Guo, C. Cao, X. Wang, X. Song, W. Wang, D. Yang, L. Xi, X. Mou and X. Dong, *Biomaterials*, 2021, **275**, 120918.
17 L. Sun, J. Wang, J. Liu, L. Li and Z. P. Xu, *Small Struct.*, 2021, **2**, 2000112.
18 Y. Yang, W. Zhu, Z. Dong, Y. Chao, L. Xu, M. Chen and Z. Liu, *Adv. Mater.*, 2017, **29**, 1703588.
19 L. Huang, Y. Li, Y. Du, Y. Zhang, X. Wang, Y. Ding, X. Yang, F. Meng, J. Tu, L. Luo and C. Sun, *Nat. Commun.*, 2019, **10**, 4871.
20 I. Sagiv-Barfi, H. E. K. Kohrt, D. K. Czerwinski, P. P. Ng, B. Y. Chang and R. Levy, *Proc. Natl. Acad. Sci. U. S. A.*, 2015, **112**, E966–E972.
21 Y. Yang, W. Zhu, Z. Dong, Y. Chao, L. Xu, M. Chen and Z. Liu, *Adv. Mater.*, 2017, **29**, 1703588.
22 C. Zhang and K. Pu, *Small Struct.*, 2020, **1**, 2000026.
23 K. Zhang, X. Meng, Y. Cao, Z. Yang, H. Dong, Y. Zhang, H. Lu, Z. Shi and X. Zhang, *Adv. Funct. Mater.*, 2018, **28**, 1804634.
24 C. Chu, E. Ren, Y. Zhang, J. Yu, H. Lin, X. Pang, Y. Zhang, H. Liu, Z. Qin, Y. Cheng, X. Wang, W. Li, X. Kong, X. Chen and G. Liu, *Angew. Chem., Int. Ed.*, 2019, **58**, 269–272.
25 S. Yu, Y. Zhou, Y. Sun, S. Wu, T. Xu, Y. Chang, S. Bi, L. Jiang and J. Zhu, *Angew. Chem., Int. Ed.*, 2021, **60**, 5948–5958.
26 J. Kim, J. Kim, C. Jeong and W. J. Kim, *Adv. Drug Delivery Rev.*, 2016, **98**, 99–112.
27 J. A. Kulkarni, D. Witzigmann, S. B. Thomson, S. Chen, B. R. Leavitt, P. R. Cullis and R. van der Meel, *Nat. Nanotechnol.*, 2021, **16**, 630–643.
28 L. Naldini, U. Blomer, P. Gallay, D. Ory, R. Mulligan, F. H. Gage, I. M. Verma and D. Trono, *Science*, 1996, **272**, 263–267.
29 J. Zhuang, H. Gong, J. Zhou, Q. Zhang, W. Gao, R. H. Fang and L. Zhang, *Sci. Adv.*, 2020, **6**, eaaz6108.
30 Y. Cheng, C. Sun, R. Liu, J. Yang, J. Dai, T. Zhai, X. Lou and F. Xia, *Angew. Chem., Int. Ed.*, 2019, **58**, 5049–5053.
31 J. Yu, D. Javier, M. A. Yaseen, N. Nitin, R. Richards-Kortum, B. Anvari and M. S. Wong, *J. Am. Chem. Soc.*, 2010, **132**, 1929–1938.
32 N. Chaudhary, D. Weissman and K. A. Whitehead, *Nat. Rev. Drug Discovery*, 2021, **20**, 817–838.
33 D. Hu, L. Chen, Y. Qu, J. Peng, B. Chu, K. Shi, Y. Hao, L. Zhong, M. Wang and Z. Qian, *Theranostics*, 2018, **8**, 1558–1574.
34 C. Zhang, Y. Yong, L. Song, X. Dong, X. Zhang, X. Liu, Z. Gu, Y. Zhao and Z. Hu, *Adv. Healthcare Mater.*, 2016, **5**, 2776–2787.
35 X. Zeng, M. Luo, G. Liu, X. Wang, W. Tao, Y. Lin, X. Ji, L. Nie and L. Mei, *Adv. Sci.*, 2018, **5**, 1800510.
36 H. Kim and W. J. Kim, *Small*, 2014, **10**, 117–126.
37 S. K. Alsaiari, S. Patil, M. Alyami, K. O. Alamoudi, F. A. Aleisa, J. S. Merzaban, M. Li and N. M. Khashab, *J. Am. Chem. Soc.*, 2018, **140**, 143–146.
38 Y. Li, K. Zhang, P. Liu, M. Chen, Y. Zhong, Q. Ye, M. Q. Wei, H. Zhao and Z. Tang, *Adv. Mater.*, 2019, **31**, 1901570.
39 J. He, T. Peng, Y. Peng, L. Ai, Z. Deng, X.-Q. Wang and W. Tan, *J. Am. Chem. Soc.*, 2020, **142**, 2699–2703.
40 P. Xue, R. Yang, L. Sun, Q. Li, L. Zhang, Z. Xu and Y. Kang, *Nano-Micro Lett.*, 2018, **10**, 74.
41 Y. Li, P. Zhao, T. Gong, H. Wang, X. Jiang, H. Cheng, Y. Liu, Y. Wu and W. Bu, *Angew. Chem., Int. Ed.*, 2020, **59**, 22537–22543.